

Original Article

Anodic electrochemical dissolution behaviors of SUS304 stainless steel and its surface characteristics by scanning electrochemical machining

Jing Wang^{a,b,c,*}, Wenyun Li^{a,b,c}, Xiaokang Yue^d, Zhongkai Ren^{a,b,c,*}

^aCollege of Mechanical Engineering, Taiyuan University of Technology, Taiyuan, Shanxi, China

^bEngineering Research Center of Advanced Metal Composites Forming Technology and Equipment, Ministry of Education, Taiyuan University of Technology, Taiyuan, Shanxi, China

^cState Key Laboratory of Metal Forming Technology and Heavy Equipment, Taiyuan, Shanxi, China

^dSchool of Mechanical Engineering, Hefei University of Technology, Hefei, Anhui, China

ARTICLE INFO

Keywords:

Dissolution characteristics
Electrochemical machining
Surface characteristics
Surface roughness
SUS304 strip

ABSTRACT

The ultra-thin SUS304 strip is a key material for various engineering applications, including aerospace and electronic communication, due to its excellent corrosion resistance and machining precision. Cold rolling is the primary method for machining the SUS304 strip; however, as the thickness decreases, surface processing defects can emerge, resulting in low surface quality and affecting the properties of the SUS304 strip. Existing methods cannot simultaneously achieve low cost, high quality, and high efficiency. In this study, scanning electrochemical machining (SECM) was adopted to efficiently and cost-effectively improve machining quality through the straight reciprocating motion of the cathode. First, the anodic dissolution characteristics of SUS304 stainless steel immersed in 10 wt% NaNO₃ solution at 298.15 K were investigated, confirming the effectiveness of NaNO₃ as an electrolyte for SECM. It was found that high current density can result in low surface roughness. Subsequently, the SUS304 strip is machined by SECM. The machined surface is compared with that produced by cold rolling from four aspects. The results show that SECM significantly reduces surface roughness Sa and Sz, with reductions of 85.5% and 79.2%, respectively. Moreover, the surface hardness, residual stress, and frictional wear are essentially the same as those of the strip processed by cold rolling. These findings validate that SECM can be used to improve the surface characteristics of SUS304 strip after cold rolling.

1. Introduction

In the aerospace industry, SUS304 ultra-thin strip, a high-end raw material, is used in the core components and parts of aircraft structures due to its superior strength and corrosion resistance. These include bodies and wings [1]. SUS304 strip is primarily processed through cold rolling [2]. Due to the plastic deformation of the material and the roughness and hardness of the roll surface, a rolling texture forms on the surface of the workpiece, resulting in low surface roughness of the SUS304 strip [3]. Critical parts in aircraft structures require high machining accuracy; otherwise, it can affect fatigue performance, corrosion resistance, and the overall lifetime of the aircraft [4]. Therefore, the surface roughness of the SUS304 strip during production is subject to very strict criteria.

To effectively reduce the surface roughness of SUS304 strip, researchers have employed silicon nitride ceramic rollers during processing. As a result, the roughness value of the SUS304 strip decreased by 10.25%, and the surface peak-valley steepness was reduced by 17.17% [5]. However, silicon nitride ceramic rollers are brittle, difficult to fabricate, and have limited corrosion resistance, complicating their application. Some researchers have combined rolling with other energy fields. For instance, Wang *et al.* proposed a method that combined pulse current with cold rolling [6], and also applied ultrasonic vibration to rolling [7]. The results from these studies were satisfactory. However, when combining rolling with other

energy fields, achieving improvements in the surface quality of SUS304 strips becomes particularly challenging once the thickness reaches the micrometer level, due to the material's mechanical properties. This increased process complexity also leads to higher processing costs [8].

Subtractive manufacturing methods, including traditional mechanical processing, electrical discharge machining, laser processing, ultrasonic machining, electron beam machining, and electrochemical machining (ECM), have been considered to further enhance the quality of SUS304 strips processed by cold rolling. Shu *et al.* used milling to machine thin-walled sheet components with variable thickness and complex curved surfaces after plastic forming, thereby enhancing machining accuracy [9]. However, traditional mechanical processing results in tool wear and high residual stress, making it difficult to simultaneously achieve high quality, low cost, and high efficiency, especially when machining wide or ultra-thin SUS304 strips. Lautre and Dharmik employed wire electrical discharge machining to precisely cut electrical steel sheets coated with insulation [10]. Unfortunately, electrical discharge can result in surface defects such as heat-affected zones and recast layers. Zhou *et al.* proposed a novel method involving fiber laser irradiation in a chemical solution to process microstructures on thin sheets made of nickel-based superalloys. This method achieved high-quality fabrication of complex microstructures [11]. However, laser processing removes surface material point by point, leading to low efficiency. Teng *et al.* combined ultrasonic machining with the blade dicing method, significantly improving machining quality compared

*Corresponding authors:

E-mail addresses: wangjing02@tyut.edu.cn (J. Wang), zhongkai_0808@126.com (Z. Ren)

Received: 28 July, 2025 Accepted: 05 November, 2025 Epub Ahead of Print: 21 February, 2026 Published: 02 April, 2026

DOI: 10.25259/AJC_887_2025

This is an open-access article distributed under the terms of the Creative Commons Attribution-Non Commercial-Share Alike 4.0 License, which allows others to remix, transform, and build upon the work non-commercially, as long as the author is credited and the new creations are licensed under the identical terms.

to conventional dicing techniques [12]. Nevertheless, ultrasonic machining has low efficiency due to its small amplitudes. Tarafder *et al.* applied electron beam machining to fabricate microstructures on 316L austenitic stainless steel, achieving good mechanical properties in the workpiece [13]. Nonetheless, electron beam machining equipment is expensive and has not yet achieved industrial-scale application for SUS304 strip machining. Compared to the aforementioned methods, ECM offers advantages such as no tool wear, no recast layers, no surface micro-cracks, low processing cost, and high efficiency [14]. Thus, ECM plays a significant role in SUS304 strip machining and is being adopted to improve strip quality.

In the ECM process of SUS304 strip, the type of electrolyte is of great importance. It directly affects the electrochemical dissolution behavior of SUS304 strip processed by cold rolling and ultimately determines the surface characteristics of the final product [15]. To identify the optimal electrolyte for the ECM process, numerous researchers have investigated the effects of various electrolyte solutions. These include acidic electrolytes such as HF, HNO₃, H₃PO₄, and HCl, as well as alkaline electrolytes such as NaOH and NH₃. However, these electrolytes pose challenges, including environmental pollution and harmful machining localization [16]. To overcome these issues, research efforts have focused on replacing acidic and alkaline solutes with organic alternatives. K3Cit, a non-toxic, non-corrosive, and environmentally friendly electrolyte, produces electrolysis byproducts with high solubility in water, accelerating the removal of electrolytic products and improving the stability of ECM. It is also favored for its ability to suppress stray corrosion [17]. However, the K3Cit solution is consumed during ECM and cannot be recycled, preventing its industrial application. NaNO₃ is an inexpensive, eco-friendly, and recyclable electrolyte that effectively addresses the limitations of other electrolytes and is widely used in ECM for various products [18]. The electrochemical behavior of materials plays a vital role in refining, adjusting current density parameters, and devising machining path strategies. Currently, the dissolution behavior of stainless steel in NaNO₃ aqueous solution has been studied. Wang *et al.* investigated the anodic dissolution of stainless steel immersed in NaNO₃ at specific temperatures and concentrations [19], Zhu *et al.* examined the dissolution behavior of 304 stainless steel in NaNO₃ at low current density [20], while Zhao *et al.* used plasma electrochemical polishing to process SUS304 and effectively eliminated the stray oxidation layer [21]. However, the application of utilizing NaNO₃ aqueous solution in scanning electrochemical machining (SECM) of micron-level SUS304 strips, where machining is carried out via straight reciprocating motion of the cathode, has not been fully explored [22]. In particular, the ranges of machining voltage and current density in SECM of SUS304 strips that can realize micron-level removal and achieve lower surface roughness are not known. In addition, there is a lack of detailed analysis on how NaNO₃-based SECM affects surface characteristics such as surface hardness, residual stress, friction, and wear in SECM of SUS304. This analysis is needed to ensure that this method does not affect or can even enhance the mechanical properties of SUS304 stainless steel after cold rolling. The above are the major obstacles to the industrialization of this process. Therefore, a comprehensive investigation into the anodic dissolution behavior of SUS304 stainless steel in the rolled state within NaNO₃ solution is essential for obtaining the appropriate processing parameters for SECM of SUS304 strips. Subsequently, through experiments, understanding how NaNO₃-based SECM influences the surface characteristics of SUS304 strips is key to improving processing quality and enabling the industrial adoption of ECM for SUS304 strips.

In this study, to enhance processing performance and clarify the forming mechanisms of SUS304 strips SECM, we investigated the dissolution behavior of SUS304 stainless steel in its rolled state in a 10 wt% NaNO₃ aqueous solution at 298.15 K. Subsequently, ECM experiments were conducted using custom-designed SECM equipment. Surface hardness, residual stress, friction and wear, and surface roughness were measured to evaluate the surface characteristics of the SUS304 strip processed by SECM in NaNO₃. Finally, the influence of NaNO₃-based SECM on these surface characteristics was analyzed. The results of this research provide new insights into the high-quality production of SUS304 strips and support the advancement of ECM for industrial use.

2. Materials and Methods

2.1. Material preparation

In this study, SUS304 stainless steel (06Cr19Ni10) with a density of 7.93 g·cm⁻³ was utilized as the anode material; it was mainly produced by cold rolling. The chemical composition of the tested surface was presented as follows: The atomic percentages of Cr, Ni, and C were 17.81%, 6.03%, and 0.07%, respectively. Through the wire electrical discharge machining, SUS304 stainless steel were cut into cubic specimens with a measuring size of 10 mm×10 mm×5 mm, and connected using a copper conductor. They were subsequently embedded in epoxy resin, with five of their sides covered. This configuration left a 10 mm × 10 mm surface area open for the examination of the anodic dissolution process.

NaNO₃, a non-linear electrolyte, offers the benefits of improving the localization effect and enhancing machining performance. Consequently, a NaNO₃ solution represents a superior and economical option for the high-quality SECM of SUS304 strips. Thus, the experimental medium used was a NaNO₃ solution, and the electrolyte solution was prepared with 10 wt% NaNO₃ in solutions at 298.15 K [23].

2.2. Electrochemical measurements

An electrochemical workstation (CHI660E, Chenhua, China) equipped with a standard three-electrode setup was used to examine the electrochemical behavior of the SUS304 stainless steel in a 10 wt% NaNO₃ solution at 298.15 K (ambient temperature). The three-electrode setup consisted of a working electrode made from SUS304 stainless steel, a platinum counter electrode, and a reference electrode utilizing a saturated calomel electrode. An electrochemical cell featuring a double-layer design was utilized for the electrochemical measurements. The inner layer of the cell comprised a NaNO₃ solution and a three-electrode system, whereas the outer layer was composed of an external circulating water system with a constant temperature. The constant temperature water tank was utilized to accurately heat and regulate the temperature of the NaNO₃ solution necessary for the ECM experiment.

Initially, the SUS304 stainless steel underwent cathodic polarization at a voltage of -1.5 V for 600 s to eliminate the passive film that had formed in the air. Subsequently, the open-circuit potentials (OCP) of SUS304 stainless steel in a 10 wt% NaNO₃ solution were measured for 3600 s to ensure stability. Following this, the potentiodynamic polarization was initiated, starting from -1.5 V and increasing to 2.5 V at a linear scanning speed of 1 mV/s. Electrochemical parameters, including the corrosion current density (i_{corr}), passivation current density (i_{pass}), passivation zone (ΔE_{pass}), corrosion potential (E_{corr}), and onset potential of transpassive dissolution (E_{trans}), were derived from the polarization curves. Electrochemical impedance spectroscopy (EIS) was conducted with a 5 mV AC perturbation over a frequency range from 100 kHz to 10 mHz to elucidate the physical structure of the passivation film. The data analysis was conducted by the Zview software. Prior to the EIS measurement, SUS304 stainless steel samples were immersed in the 10 wt% NaNO₃ solution for 1800 s to ensure the establishment of the stable passivation film. Ultimately, the composition of passive film was analyzed with the aid of an AXIS SUPRA+ spectrometer (AXIS Supra™, Kratos, Japan). The XPS peaks acquired from the analysis were referenced to the standard peak (C 1s, 284.8 eV), and the XPS data were subsequently processed and analyzed with the aid of Thermo Advantage software.

The surface characteristics of SUS304 strips machined by ECM were evaluated from four aspects: surface roughness, hardness, residual stress, and friction and wear. Surface roughness (Ra, Sa, Sz) was measured using a confocal laser scanning microscope (VK-X200K, Keyence, Japan). For each sample, three distinct surface areas were selected for measurement, and the average value was used to represent the surface roughness of each sample. Hardness was determined using a digital Vickers microhardness tester (MHV-50Z/V3.0, SCTMC, China). Five evenly spaced points on the specimen surface were selected for measurement, and the average value was used to represent the specimen's hardness. The test was conducted with a load of 20 kg applied for 10 seconds. Residual stress was measured using X-ray diffraction with the tilt method. The measurement point was located

at the center of the sample's testing zone. A diffractometer (Bruker D8 Discover, China) equipped with a high-throughput microbeam source was used. The X-ray tube operated at 40 kV and 0.5 mA. A Co target was used, emitting $K\alpha$ radiation with a wavelength of 1.78897 Å. The diffraction angle range for stress evaluation was 86° to 93°. A Poisson's ratio of 0.29 and an elastic modulus of 193 GPa were used in stress calculations. Friction and wear were assessed using a high-frequency reciprocating rig (HFRR) system (WDF-300, Zhongkekaihua, China). The tests were conducted using Cr15 steel ball heads with a diameter of 6 mm. Test parameters included a 5 N static load, 15 min of wear time, an 8 mm stroke length, and a frequency of 1 Hz under dry contact conditions.

2.3. ECM experimental apparatus

ECM tests of SUS304 stainless steel in 10 wt% NaNO_3 aqueous solution were executed with varying current densities employing a bespoke experimental system (Figure 1). The experimental system included a special fixture, a power supply, an electrolyte circulation-filtration module, a thermostat, and a motion control unit. The cathode made of SUS304 stainless steel was interconnected with the adjustment device via the cathode rod assembly. The machining gap between the cathode and anode was initially set with exactness through manual motor operation, at a value of 0.5 mm. In the course of the ECM experiments, the electrolyte circulation supply unit provided a 10 wt% NaNO_3 solution that was clean and under a set pressure, which flowed from the inlet to the outlet through the machining zone. It also filtered and removed any dirty electrolyte, primarily consisting of reaction heat and bubbles. Experiments to evaluate current efficiency were performed under a constant current setting, achieving current densities from 1 to 15 A/cm^2 between the SUS304 stainless steel substrate and the cathode. The specimens of SUS304 stainless steel were weighed on a high accuracy electronic balance (ME204E, Mettler Toledo, Switzerland) before and after each experiment run. The current efficiency (η) of the SUS304 stainless steel is associated with the actual mass loss (ΔM), the theoretical mass electrochemical equivalent (ω), the current (I), and dissolution duration (t), which can be articulated as follows (Eq. 1):

$$\eta = \Delta M / \omega It \quad (1)$$

After the ECM processing was finished, the specimen surfaces were assessed for the surface topography, the elemental composition, and the surface roughness using a confocal laser scanning microscope, a scanning electron microscope (SEM, JOEIT500, JEOL Ltd, Japan), and an energy dispersive X-ray spectroscope (EDX, X-max, Oxford, UK).

3. Result and Discussion

3.1. Electrochemical characterization

To understand the dissolution behavior of SUS304 stainless steel, the microstructure was analyzed before electrochemical testing and ECM experiments. Figure 2(a) shows the microscopic surface morphology of SUS304 stainless steel. The micrograph evidently demonstrates that the austenite grains are uniformly distributed in general. Lamellar twin structures are scattered within the austenite matrix, and no significant inclusion clustering is noticed. The macroscopic morphological features of the matrix are clearly exhibited. For a further examination of the grain-size distribution and crystallographic orientation of SUS304 stainless steel, electron back scatter diffraction (EBSD) imaging is conducted. Figures 2(b, c) show the EBSD data, including the band contrast (BC) image and the inverse-pole-figure (IPF) map. The BC image distinctly presents the austenitic microstructure of the SUS304 stainless steel, as well as twins and many fine grains, which is in line with the aforementioned characteristics. The IPF map shows that the grains in the SUS304 stainless steel are randomly oriented and completely austenitic. The fine grains possess a thicker, denser, and more stable passive film, which affects electrochemical dissolution behavior and may enhance corrosion resistance.

The corrosion characteristics of SUS304 stainless steel in a 10 wt% NaNO_3 solution at 298.15 K were evaluated using electrochemical methods, including open circuit potential and potentiodynamic polarization. The E_{ocp}^r curve for SUS304 stainless steel immersed in 10 wt% NaNO_3 at 298.15 K has been shown in Figure 2(d). E_{ocp}^r was monitored for 60 min. The curve indicates that the potential gradually stabilizes over time, which is attributed to the formation of a passive film on the surface. The stabilized potential was approximately -0.038 V.

The polarization curve for SUS304 stainless steel has been shown in Figure 2(e). It reveals a typical active-passive-transpassive behavior.

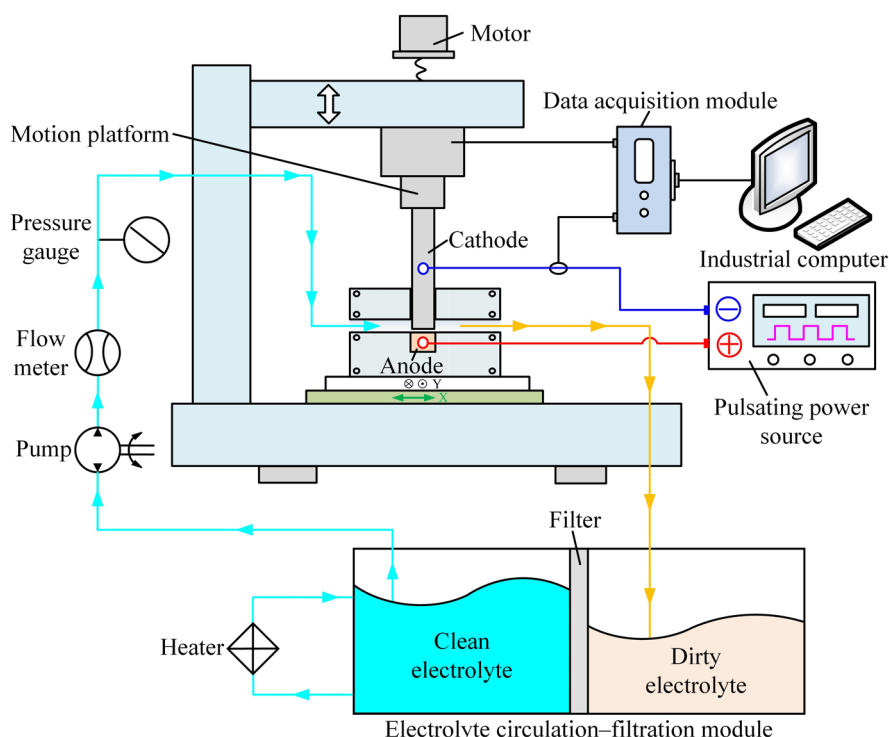


Figure 1. Schematic diagram of the ECM system.

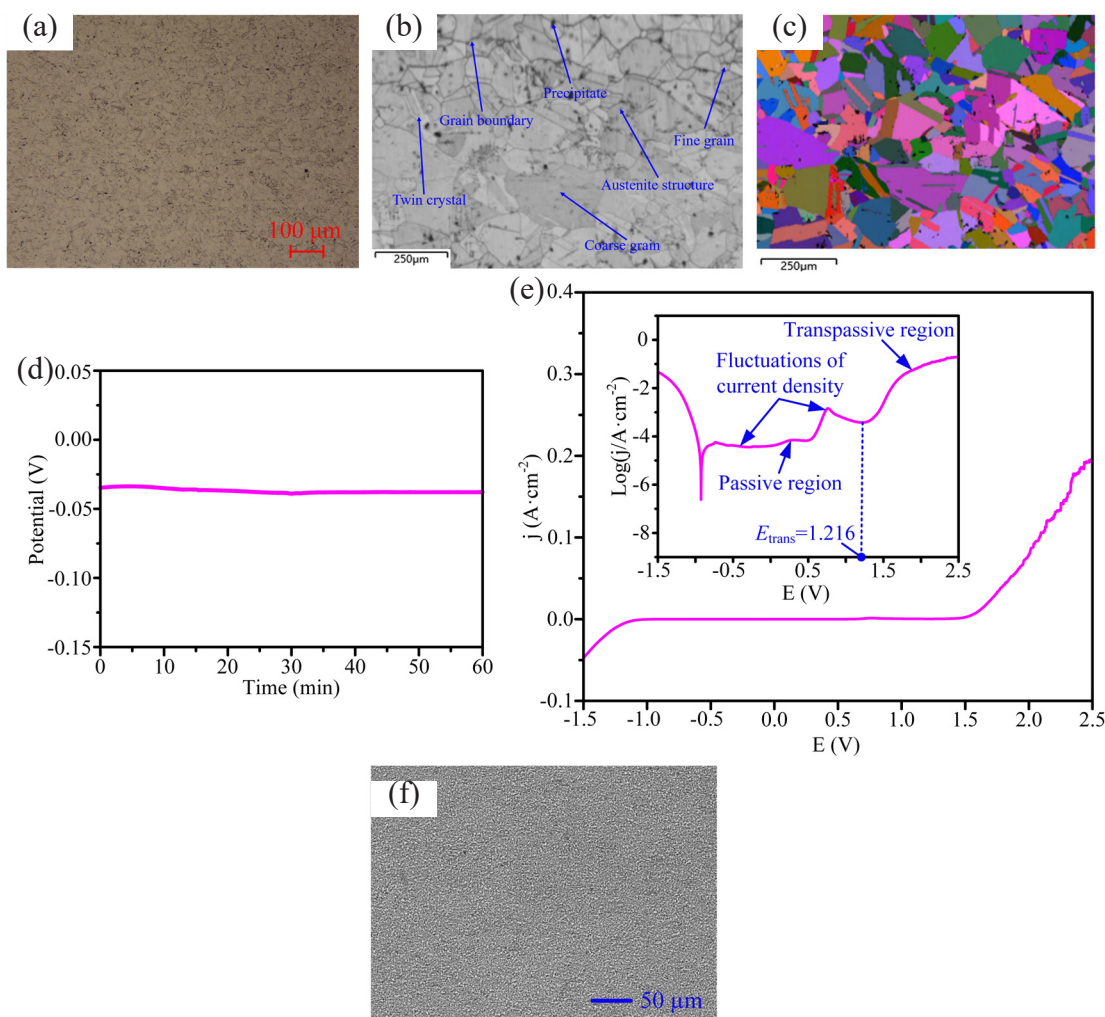
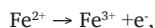


Figure 2. Metallographic image of SUS304 stainless steel prior to polarization curve tests, open circuit potential–time curve and polarization curve of SUS304 stainless steel immersed in a 10 wt% NaNO₃ solution at 298.15 K: (a) metallographic image; (b) band contrast image; (c) inverse pole figure image; (d) open circuit potential–time curve; (e) polarization curve; and (f) SEM image after polarization curve tests.

In the passive region, the current density remains nearly constant due to the formation of a passive layer that inhibits the ECM process. Once the potential exceeds the breakdown potential (E_{trans} , approximately 1.216 V), the material enters the transpassive region, where extensive dissolution of the metal matrix occurs. A near-linear relationship between polarization potential and current density is observed in this region, indicating a progressive decline in passive film stability as current density increases. Moreover, a single current peak exists in the passive region. This phenomenon occurs because the non-metallic MnS inclusions on the surface of SUS304 stainless steel result in preferential corrosion around the particles during the polarization test [24]. For potentials beyond E_{trans} , corresponding to passive film breakdown, the dominant anodic reactions can be described based on the iron-based alloy composition of SUS304 stainless steel [19]:



Furthermore, at the anode, the reaction of oxygen evolution occurs simultaneously [19]:



Furthermore, SEM was used to examine the electrochemical dissolution morphology of SUS304 stainless steel after polarization tests, as shown in Figure 2(f). The images indicate that corrosion in the 10 wt% NaNO₃ solution at 298.15 K was uniform.

3.2. Analysis of passive layer composition

The results in Section 3.1 indicated the formation of a passive layer on the machined surface of SUS304 stainless steel after immersion in a 10 wt% NaNO₃ aqueous solution at 298.15 K. Therefore, this study proceeded to characterize the surface composition of the passive layer formed on SUS304 stainless steel in this corrosive environment using XPS. The XPS spectrum has been shown in Figure 3(a) and displays peaks corresponding to Fe 2p, Cr 2p, Ni 2p, O 1s, and C 1s.

Detailed spectral analysis of these primary elements is presented. In Figure 3(b), the Fe 2p spectrum shows two peaks at binding energies (BEs) of 725.2 eV and 710.6 eV, corresponding to Fe₂O₃. Peaks at 723.4 eV and 708.9 eV correspond to Fe⁰, while those at 719.9 eV and 706.5 eV correspond to FeO, with satellite peaks at 728.9 eV and 712.7 eV. The Cr 2p spectrum in Figure 3(c) shows peaks at 585.6 eV and 575.8 eV, attributed to Cr₂O₃; peaks at 583.1 eV and 573.7 eV indicating metallic Cr; and peaks at 587.2 eV and 577.2 eV associated with CrO₃. In Figure 3(d), the Ni 2p spectrum displays two peaks at BEs of 856.7 eV and 874.5 eV, corresponding to Ni(OH)₂. Additionally, two peaks at BEs of 855.4 eV and 872.9 eV, corresponding to NiO, with two satellite peaks observed at BEs of 861.3 eV and 879.4 eV. In summary, the passive layer formed on SUS304 stainless steel in the 10 wt% NaNO₃ solution is a mixture of compounds, including Fe₂O₃, FeO, Fe, Cr₂O₃, CrO₃, Cr, Ni(OH)₂, and NiO.

To further examine the quantitative distribution of the passivation layer, peak areas were calculated, and the content of Fe₂O₃, FeO, Fe, Cr₂O₃, CrO₃, Cr, Ni(OH)₂, and NiO was determined (Figure 3e). Iron

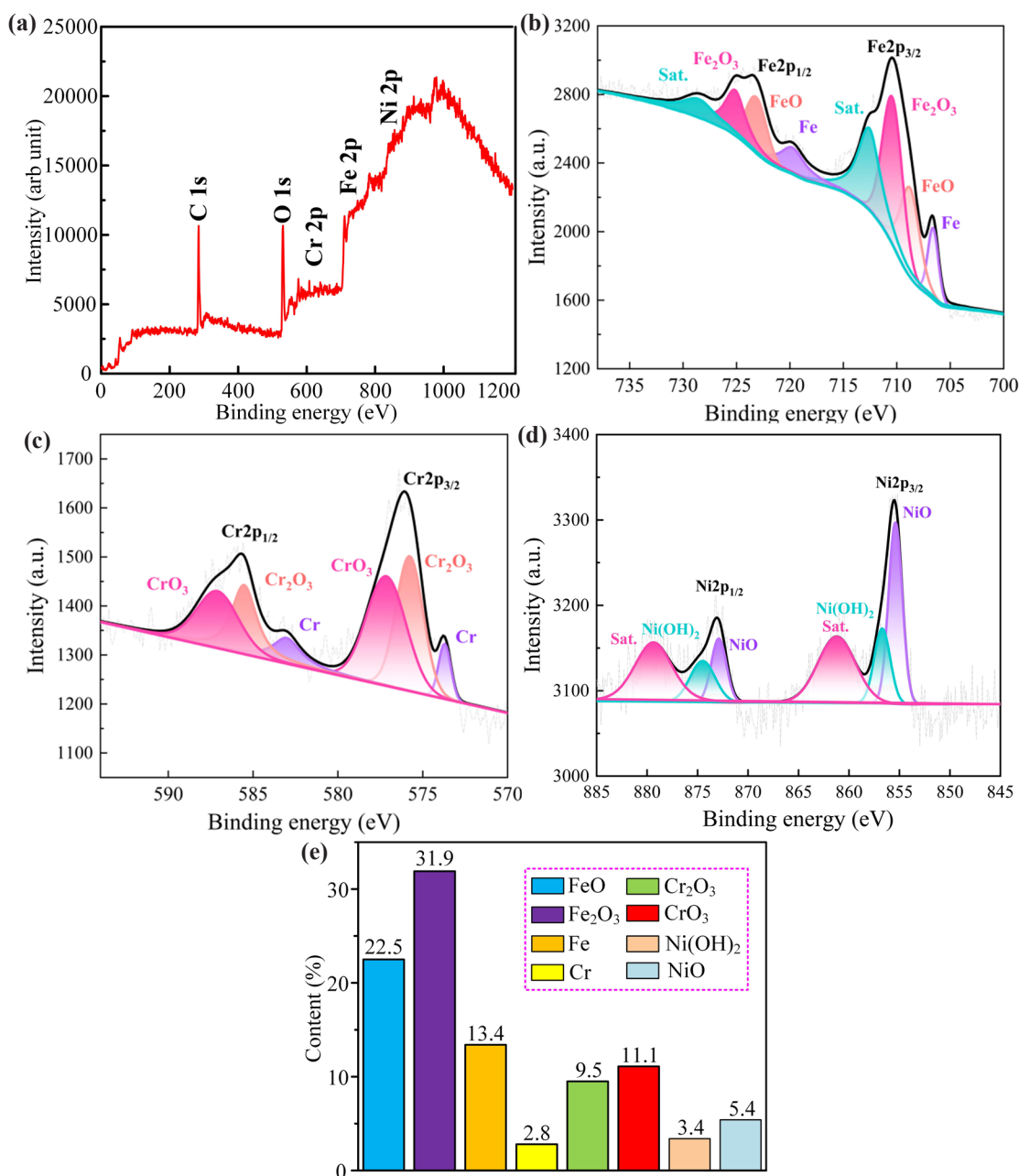


Figure 3. Composition of the passive layer formed on SUS304 stainless steel immersed in a 10 wt% NaNO₃ solution at 298.15 K: (a) XPS spectrum of the machined surface; (b) high-resolution XPS spectra for Fe 2p; (c) high-resolution XPS spectra for Cr 2p; (d) high-resolution XPS spectra for Ni 2p; and (e) quantitative distribution.

and chromium oxides are the main components of the passive layer. Iron oxides constitute 54.4 atomic percent (at%), with Fe₂O₃ as the dominant form at 31.9 at%. Chromium oxides account for 20.6 at%, with CrO₃ as the primary form, contributing 11.1 at%. Previous studies have shown that the passivation layer on machined SUS304 surfaces consists of at least two distinct layers: an inner and an outer layer [25]. Fe₂O₃ and CrO₃ are mainly found in the outer layer, while FeO and Cr₂O₃ are concentrated in the inner layer. Cr₂O₃, known for its high stability and protective properties, effectively prevents further corrosion and protects the substrate. Therefore, the compactness of the inner layer is critical to the corrosion resistance of SUS304 stainless steel. Moreover, the passivation film contains small amounts of NiO and Ni(OH)₂. NiO forms a composite oxide structure with Cr₂O₃, improving the density, adhesion, and puncture resistance of the passivation layer. Ni(OH)₂ helps reduce defect density, inhibits the dissolution of Fe and Cr, and increases the density of the passivation layer. Additionally, the XPS high-resolution spectra of Fe 2p and Cr 2p show peaks corresponding

to metallic Fe and Cr. This may be attributed to the formation of FeO in the passive film, which can introduce pores or voids within the otherwise dense Cr₂O₃ layer, allowing metallic signals from the substrate to appear.

3.3. Analysis of passive layer structure

EIS was also conducted to assess the physical structure of the passivation film on the machined SUS304 surface after immersion in a 10 wt% NaNO₃ solution at 298.15 K. The results are shown in Figure 4, presenting impedance spectra as Nyquist and Bode plots. In the Nyquist plot (Figure 4a), capacitive arcs are observed with a typical semicircular configuration, indicating a capacitive response from the passivation layer [26]. The Bode impedance diagram (Figure 4b), with fitting curves shown in red, demonstrates that the impedance magnitude decreases sharply with increasing frequency, indicating strong corrosion resistance of the passivation film. This is primarily

attributed to the presence of the highly corrosion-resistant Cr_2O_3 layer. The Bode phase plot (Figure 4b), with fitting curves in blue shows that the impedance modulus at high and low frequencies corresponds to the solution resistance and polarization resistance, respectively. Multiple peak phase angles observed in the SUS304 sample suggest several time constants, implying complex charge transfer processes at the electrolyte/electrode interface related to the passivation film. In the Bode phase plot, two peaks are observed, which correspond to two time constants. According to the features of the Nyquist plots, an electrochemical equivalent circuit with two constant phase elements is employed, and the fitted data obtained have been listed in Table 1. The components of this circuit represent the electrochemical behavior of SUS304 stainless steel. In this EEC, the chi-square values (χ^2) of the equivalent circuit are below 3.7×10^{-3} , showing that the fitted data fit the proposed equivalent circuit well. Specifically, R_s stands for the solution resistance, R_f represents the film resistance, and R_{ct} refers to the charge transfer resistance. Generally, a passivation film with a compact and stable structure has a high R_f . The fitting result in this study shows that the R_f value reaches as high as $176210 \Omega \cdot \text{cm}^2$, indicating that the passive film formed on SUS304 stainless steel after electrochemical treatment in 10 wt% NaNO_3 electrolyte has excellent corrosion resistance. CPE is the constant phase element. CPE_f corresponds to the capacitance related to the film resistance in the high-frequency region, and CPE_{dl} denotes the electric double-layer capacitance. Q_f and Q_{dl} respectively represent the diffusion abilities of ionic species and the capacitance at the electrode/solution interface, respectively. Normally, a smaller Q_f indicates greater hindrance to the current flow process, suggesting increased resistance of the passive layer to ionic penetration. The fitting result of Q_f is as low as $7.83 \times 10^{-5} (\Omega^{-1} \cdot \text{cm}^{-2} \cdot \text{s})$, indicating that the passive film formed on SUS304 stainless steel after ECM in 10 wt% NaNO_3 electrolyte has higher resistance to ion penetration. R_f and R_{ct} are connected in series, and the sum of R_f and R_{ct} represents the total corrosion resistance (R_p) at the interface between the electrolyte and the material. A higher R_p means it is more difficult for redox reactions to occur between the material and the electrolyte, implying a more

compact and stable structure of the material. The fitting result shows that the value of R_p is approximately equal to that of R_f (as high as $176210 \Omega \cdot \text{cm}^2$), indicating that the passive film formed on SUS304 stainless steel after ECM in 10 wt% NaNO_3 electrolyte has a relatively stable and compact structure. The value of n is the exponent of the CPE, a dimensionless parameter that describes the extent to which the behavior of the CPE element deviates from that of an ideal capacitor. The value of n ranges from 0 to 1, reflecting the degree of this effect. When n approaches 0, the element behaves more like a pure resistor, while when n approaches 1, it behaves more like a pure capacitor. Moreover, previous studies indicate that as n approaches 1, it leads to surface uniformity and a denser passivation film. The fitting result in this study shows that the n_f value was 0.81, which is close to 1. Therefore, these results confirm that the SUS304 stainless steel in a 10 wt% NaNO_3 solution formed a more capacitive, thicker, and stable passive film.

Based on the outcomes of EEC analysis, schematic diagrams were suggested to depict the structure of the passive layer formed on the surface of SUS304 stainless steel in a 10 wt% NaNO_3 solution, as shown in Figure 4(c). According to XPS results, the passive layer on SUS304 stainless steel primarily consists of metal oxides, with Cr_2O_3 exhibiting a high concentration, signifying a dense and stable structure. Thus, the passive layer formed on the surface of SUS304 stainless steel in a 10 wt% NaNO_3 solution contains numerous dense and stable structures, which grants SUS304 strong corrosion resistance in the 10 wt% NaNO_3 solution.

3.4. Measurement of current efficiency

Figure 5 illustrates the current efficiency of SUS304 stainless steel as a function of current density, ranging from 1 to 40 A/cm^2 . The graph shows that current efficiency initially increases sharply and then plateaus once the current density exceeds 15 A/cm^2 . Based on this behavior, the current density range can be divided into two distinct zones: Zone I, covering current densities from 1 to 15 A/cm^2 , and Zone II, covering current densities from 15 to 40 A/cm^2 .

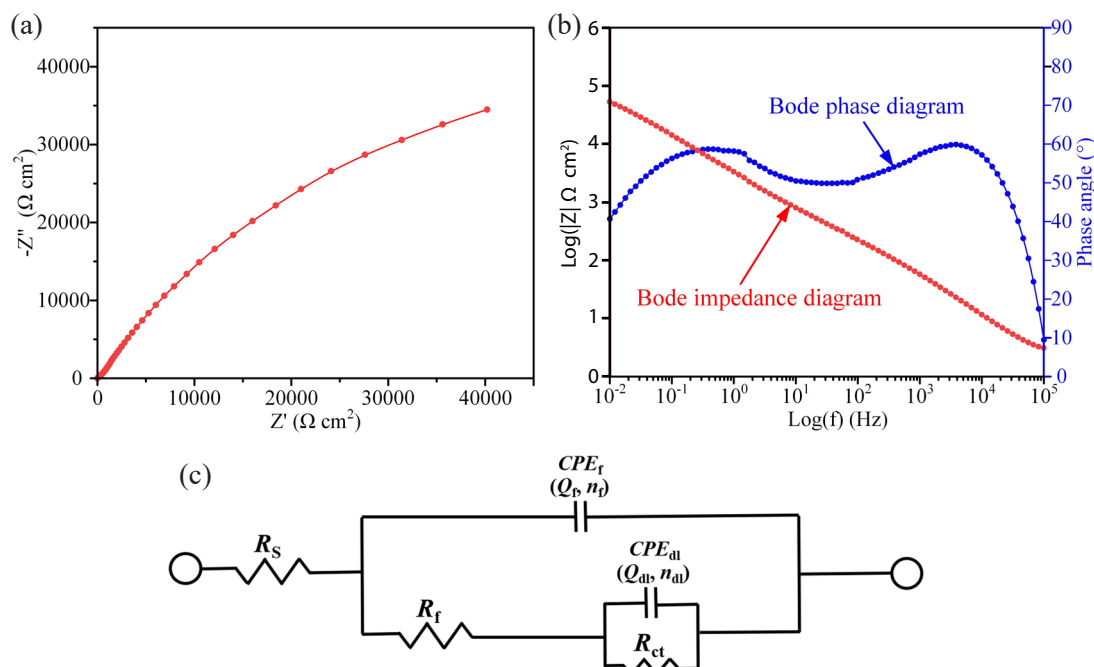


Figure 4. EIS data of SUS304 stainless steel in an immersed 10 wt% NaNO_3 solution at 298.15 K: (a) Nyquist plots; (b) Bode plots-impedance and phase angle; and (c) parallel equivalent-circuit model.

Table 1. EEC model fitting results of SUS304 in 10 wt% NaNO_3 solution at 298.15 K.

$R_s (\Omega \cdot \text{cm}^2)$	$Q_f (\Omega^{-1} \cdot \text{cm}^{-2} \cdot \text{s}^n)$	n_f	$R_f (\Omega \cdot \text{cm}^2)$	$Q_{dl} (\Omega^{-1} \cdot \text{cm}^{-2} \cdot \text{s}^n)$	n_{dl}	$R_{ct} (\Omega \cdot \text{cm}^2)$	χ^2
2.71	7.83×10^{-5}	0.81	176210	1.38×10^{-5}	0.629	246.4	3.7×10^{-3}

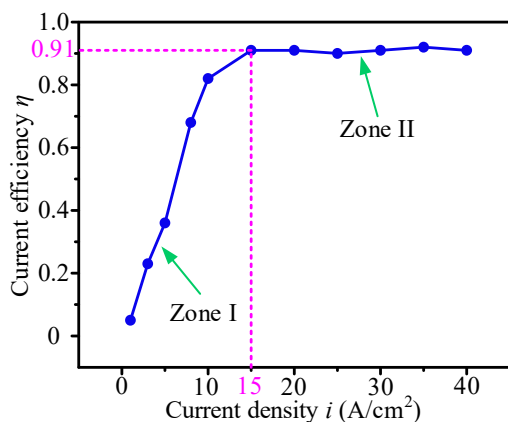


Figure 5. Current efficiency curve of SUS304 stainless steel.

II, representing the steady-state dissolution region at current densities above 15 A·cm⁻².

In Zone I, the current efficiency is relatively low, primarily due to oxygen evolution, which consumes most of the electrical energy [27]. Only a small portion of the current contributes to the dissolution of the SUS304 surface, resulting in reduced current efficiency. However, as current density increases, current efficiency rises rapidly. This suggests a transition in the dominant electrochemical reaction—from oxygen evolution to metallic dissolution. As a result, more metal is dissolved from the SUS304 surface, significantly improving current efficiency.

Zone II is characterized by efficient dissolution of the SUS304 surface, with current efficiency remaining nearly constant as current density increases. In this zone, most of the electrical power is used for anodic metal dissolution, resulting in a peak current efficiency of approximately 91%. However, this value is still below 100%, likely because a small portion of the current continues to support oxygen evolution. Therefore, Zone II is the primary region for effective surface dissolution and provides guidance for selecting optimal current densities in practical ECM applications.

3.5. Surface morphology

To further explore the anodic dissolution behavior of SUS304 stainless steel and evaluate its performance in ECM, we examined the surface morphology, chemical composition, and surface roughness of the machined surface in a 10 wt% NaNO₃ solution at 298.15 K under

varying current densities. These analyses were carried out using SEM, EDX, and a confocal laser scanning microscope.

In the experiment, six current densities (1, 3, 5, 7, 10, and 15 A·cm⁻²) were selected for comparison. Figure 6(a) shows how surface roughness (Ra) varies with current density. The results indicate that surface roughness decreases from 4.214 μm at 1 A·cm⁻² to 0.752 μm at 15 A·cm⁻². This suggests that increasing current density enhances surface quality. Therefore, SECM treatment of SUS304 in a 10 wt% NaNO₃ solution at 298.15 K can produce a smoother surface finish.

Next, the morphological characteristics of the machined surfaces in the same electrolyte are analyzed. The microstructure of the surfaces is shown in Figure 6(b-e). At a current density of 1 A·cm⁻², the surface shows numerous grooved microstructures and experiences intense localized electrochemical dissolution, resulting in many pits. As current density increases, these grooves and pits diminish rapidly. This indicates that higher current density helps to reduce unevenness in electrochemical dissolution rates across the surface. Moreover, the current density serves as the critical factor controlling the quality and stability of the passive film; it directly determines whether the surface remains passive or becomes active. At low current densities, the anodic oxidation process is slow and incomplete, resulting in the formation of a passive film with numerous structural defects (such as vacancies and grain-boundary micro-cracks). This type of film is discontinuous and has low density, enabling ions to penetrate easily and trigger pitting. As a result, the quality of the machined surfaces is poor. When the current density is increased to an optimal range, the charge-transfer efficiency per unit area increases significantly. A uniform and dense passive film is then rapidly formed. As a result, the surface reaches a stable passive state that effectively prevents both the initiation and propagation of pits, and the quality of the machined surfaces is improved. In addition, the flow in the experiment is consistent and high-speed, which quickly removes dissolution products (metal cations, oxide debris) and locally accumulated harmful ions, preventing film breakdown due to product buildup and keeping the electrolyte composition uniform. This establishes a stable environment in which the high current density can constantly facilitate the repair and growth of the passive film, ensuring long-term stability of the film [25,26]. Consequently, this contributes to the machined surface becoming progressively smoother. At 15 A·cm⁻², the corrosion grooves and pits disappear entirely, and the surface appears very smooth. Nevertheless, in the NaNO₃ solution, it is apparent that a multitude of electrolytic products are bound to the machined surface of SUS304 stainless steel, making their complete removal difficult. Thus, at a current density of 15 A·cm⁻², with only a few electrolytic products still adhering to the surface of the sample. Thus, analysis indicates that at higher current densities, the machined

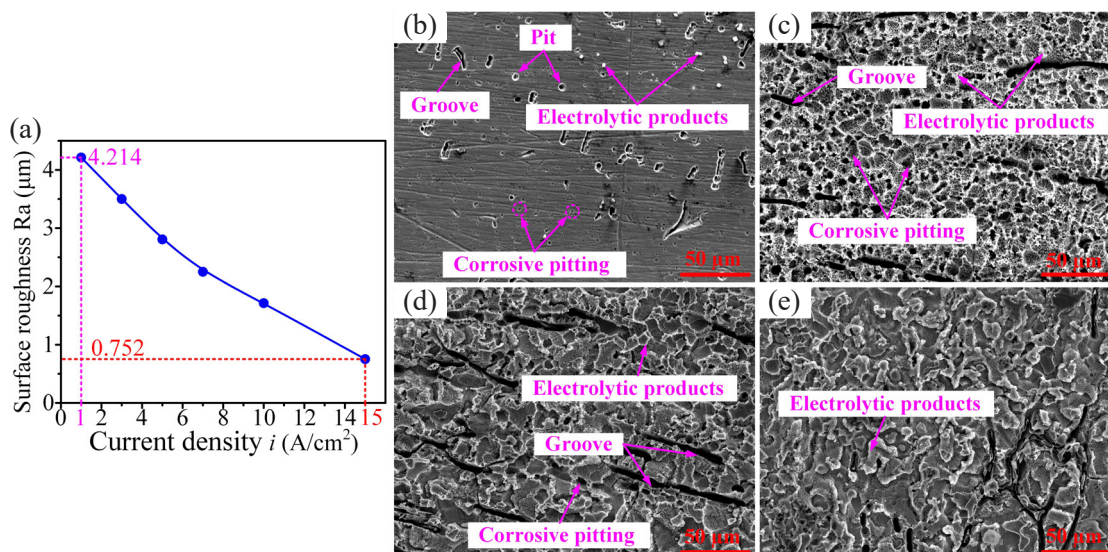


Figure 6. Change in surface roughness Ra of the machined surface with the current density (a) and dissolution morphology of the machined surface for SUS304 stainless steel immersed in 10 wt% NaNO₃ solution at 298.15 K using various current densities: (b) 1; (c) 5; (d) 10; and (e) 15 A/cm².

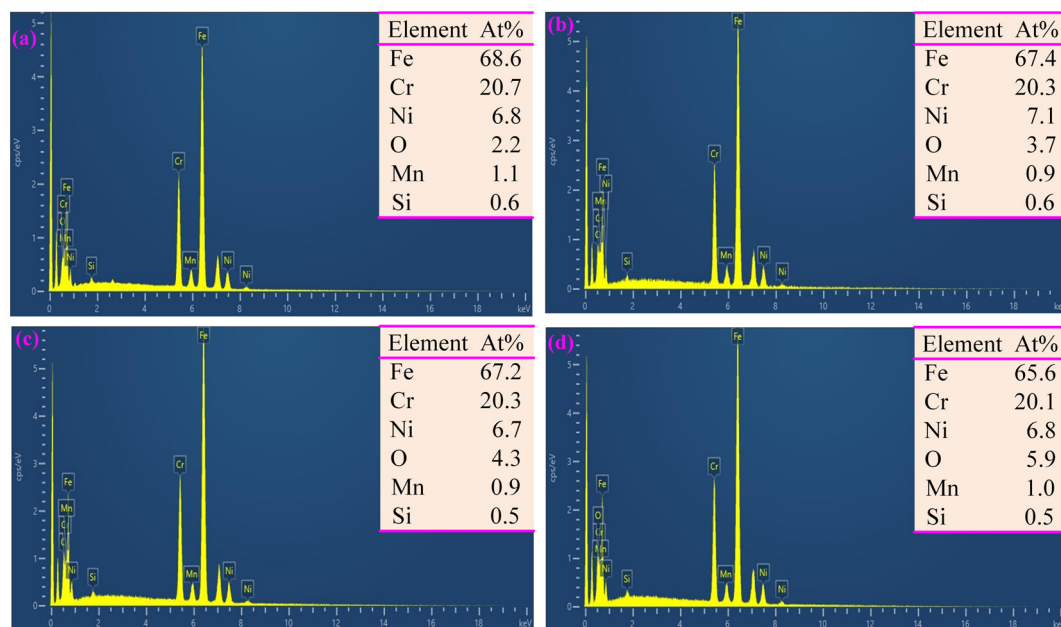


Figure 7. Chemical element composition (At%) of machined surface for SUS304 stainless steel immersed in 10 wt% NaNO_3 solution at 298.15 K using various current densities: (a) 1, (b) 5, (c) 10, and (d) 15 A/cm^2 .

surface of SUS304 stainless steel becomes more uniform, thereby enhancing surface quality.

Meanwhile, as shown in Figure 7, the results of the energy spectrum analysis reveal a somewhat higher oxygen content compared to the matrix material, indicating the presence of oxidation products. Furthermore, the oxygen content on the surface of SUS304 increases with rising current density. A plausible explanation for this phenomenon is that higher current density accelerates the oxidation reaction, resulting in the formation of more oxides on the stainless steel surface, thereby increasing the oxygen content. Furthermore, the chromium content is higher than that of the matrix material, which can be attributed to the formation of a chromium-rich oxide layer during processing. Additionally, the material's surface exhibits carbon residue. This is because the carbon in the SUS304 is insoluble. On the other hand, other alloying elements in the SUS304 (such as Fe, Cr, Ni) experience selective dissolution during the ECM process, progressively revealing the initially embedded carbon on the surface of the SUS304.

3.6. SECM of SUS304 strips in NaNO_3 solution

ECM of SUS304 strips is performed using a scanning technique. SECM has numerous significant advantages. For instance, the impact of electrolytic products on processing accuracy is minimal, ensuring a consistently uniform current density. This contributes to the even removal of the surface material of the metal strips throughout the entire machining process [22]. The SUS304 strip experiences continuous linear

reciprocating movement of the cathode. Depending on the difference in removal rates between peaks and valleys on the SUS304 surface, the surface roughness values gradually decrease. The cathode halts when the machining specifications are achieved (Figure 8a).

In subsequent research, appropriate parameters were necessary, and four aspects needed to be considered. (i) Section 3.1 provided a systematic demonstration that exceeding the voltage at the transpassive potential (1.216 V) was crucial for achieving optimal processing results. (ii) There was a steady-state dissolution region at current densities above 15 A/cm^2 . (iii) At higher current densities, the machined surface of the SUS304 stainless steel became smoother, thereby improving the surface finish. However, it was particularly important to emphasize that while higher current densities led to better surface smoothness, they also caused higher material removal rates during the SECM. The experimental protocol specifically aimed for a controlled thickness reduction of exactly 10 μm per processing pass (iv) Surface roughness requirement was set not to exceed $\text{Sa } 0.300 \mu\text{m}$, which was a critical quality standard for ensuring the functional performance of the final processed components. These process parameters were carefully optimized to achieve both the desired material removal rate and the required surface finish specifications. The appropriate parameters included an electrolyte temperature of 25 $^\circ\text{C}$, a pulse frequency of 5000 Hz, a cathode feed rate of 10 mm/min, and a machining voltage of 20 V. Additional parameters are listed in Table 2.

A custom-designed experimental setup was implemented for SECM. This setup consisted of a motion control module, a power supply, an

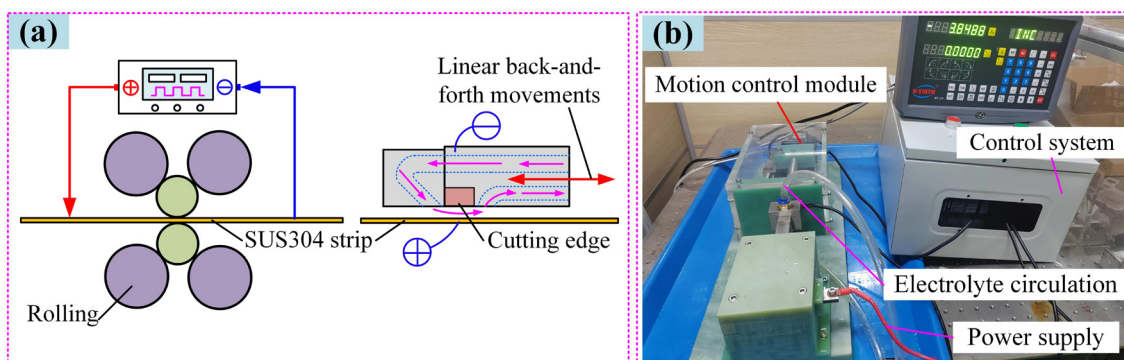


Figure 8. The process of SECM applied to SUS304 strips: (a) a diagram depicting the machining procedure; (b) a specially crafted experimental system.

Table 2. Experimental conditions for SECM of SUS304 strips.

Experimental conditions	Values
Material of the cathode	06Cr19Ni10
Material of the insulated layer for the cathode	High polymer
Material of the workpiece	06Cr19Ni10
Type and concentration of electrolyte	10 wt% NaNO ₃
Inlet velocity of electrolyte, V_{in} (m·s ⁻¹)	6
Feed depth, d (mm)	5

electrolyte circulation unit, and a machining cell. The motion control module precisely managed the platform movement (Figure 8b). The power supply delivered high-frequency pulse power and accurately controlled the experimental parameters across the two counter polarities. The electrolyte circulation unit maintained a clean flow of electrolyte at a set pressure and temperature through the machining gap. It also filtered out machining by-products from the electrolyte over time. The machining cell comprised three main components: a special fixture, a workpiece, and an integrated cathode. The fixture, made of epoxy material, offered advantages such as electrical insulation and corrosion resistance. It formed a closed flow path with the two polarities and was mounted at the base of the machining device. The workpiece was embedded in the fixture, covering five sides to ensure it remained secure during machining. The active machining area of the workpiece measured 40 mm × 20 mm. The integrated cathode, mounted on the feed axis, could move horizontally, allowing precise positioning relative to the workpiece, which is crucial for accurate machining.

The cathode featured an integrated design with cutting edges and built-in inlet and outlet flow channels, which indicates that it does not need to be frequently disassembled and reinstalled during machining. These cutting edges were essential for machining SUS304 strips. The SUS304 strips were cut into cuboids measuring 40 mm × 20 mm × 0.5 mm using wire electric discharge machining (WEDM). Following this, the samples were cleaned with alcohol in an ultrasonic cleaner prior to further experimentation.

3.6.1. Influence of SECM on quality of machined surface

Experiments were conducted to examine the impact of SECM on the quality of machined surfaces. A comparison was made between the

initial surface and the machined surface after SECM (Figure 9a). The 3D surface topography was recorded, and surface roughness values (Sa and Sz) were assessed. Initially, for the SUS304 strips, the surface roughness values of Sa and Sz were 1.437 μm and 16.184 μm, respectively (Figure 9b). After SECM machining, these values decreased to 0.208 μm and 3.361 μm, respectively, representing reductions of approximately 85.5% and 79.2% (Figure 9c). This indicates a significant improvement in machining quality. Throughout the SECM process, in accordance with electrochemical principles [28], the current density at the surface peaks of the SUS304 strips is higher, facilitating faster material removal; whereas in the valleys, the current density is lower, resulting in slower removal (Figure 9b). Consequently, this reduces the height difference between peaks and valleys on the SUS304 surface (Figure 9c), leading to reduced surface roughness values (Sa and Sz).

3.6.2. Influence of SECM on surface hardness

The surface hardness of a machined workpiece is critical for the fatigue resistance of components. Traditional machining methods often produce work-hardened layers on component surfaces [29]. However, limited research exists on how SECM affects the surface hardness of SUS304 strips. Therefore, variations in surface hardness before and after SECM were investigated. Figure 10(a) shows the hardness values before and after SECM. Before machining, the average hardness of the SUS304 strip was about 309 HV. After electrochemical treatment, it slightly increased to around 313 HV. As SECM is a non-contact process, it does not induce a work-hardened layer but rather removes any existing work-hardened layer from previous processing. Additionally, preceding ECM studies have shown that the passivation film on SUS304 surfaces primarily consists of iron oxide (Fe₂O₃) and chromium oxide (Cr₂O₃). This nanoscale film significantly enhances corrosion resistance and may also slightly increase surface hardness. The thickening of the passivation film may provide minor mechanical reinforcement, contributing to the hardness of SUS304 strips [30]. Moreover, in the SECM process with the NaNO₃ solution, the metal substrate experiences uniform dissolution under over-passivation potential, thereby avoiding localized excessive corrosion. Meanwhile, the NO₃⁻ ions supplied by NaNO₃ facilitate the swift oxidation of Cr³⁺ to Cr₂O₃, preserving the integrity of the passivation film. Consequently, the presence of NaNO₃ sustains a dynamic balance between the dissolution and regeneration of the passivation film. The above reasons may lead to the surface

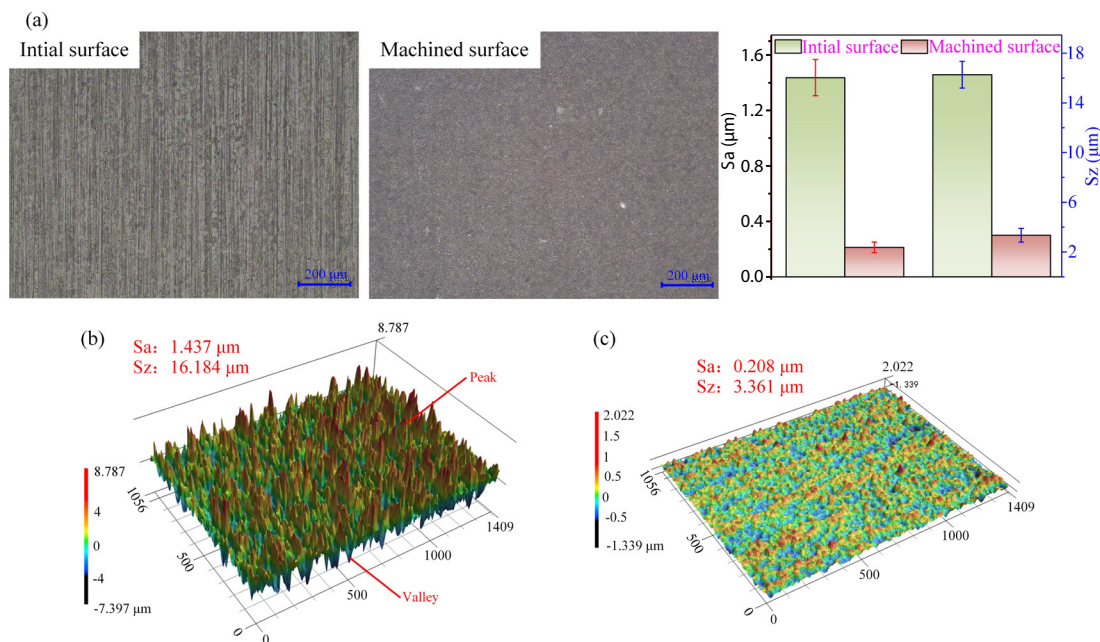


Figure 9. Roughness values and 3D surface topography for initial surface and machined surface after SECM: (a) roughness values; (b) 3D surface topography for initial surface, and (c) 3D surface topography for machined surface after SECM.

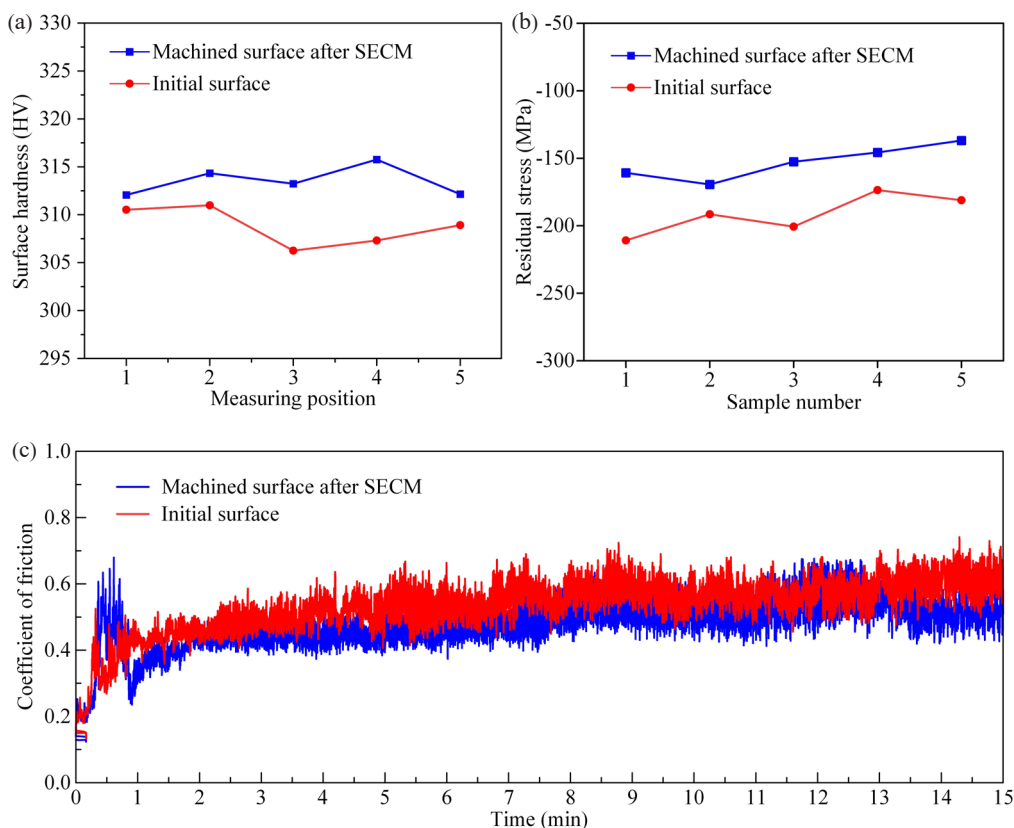


Figure 10. Surface characteristics for the initial surface and the machined surface after SECM: (a) surface hardness; (b) residual stress, and (c) distribution of the friction coefficient over time.

hardness of SECM-treated SUS304 strips being roughly equivalent to that of cold-rolled SUS304 strips.

3.6.3. Influence of SECM on residual stress

Residual stress formed during the rolling process of SUS304 strips can reduce stress corrosion resistance and fatigue life, potentially leading to cracking [31]. While traditional manufacturing processes aim to reduce surface roughness, contact-based methods may introduce additional residual stresses, adversely affecting processing quality [32]. Thus, non-contact SECM is an advisable alternative. However, limited studies have evaluated residual stress in SUS304 strips machined via SECM. It is therefore important to assess changes in residual stress before and after SECM treatment.

Figure 10(b) presents the residual stress values at various test points on SUS304 strip surfaces, before and after electrochemical treatment. During rolling, compressive residual stress is introduced due to surface cooling and constrained core shrinkage, forming a plastic deformation layer. Before SECM, the average surface residual stress was -191.56 MPa. After treatment, this decreased to -153.08 MPa, indicating a trend of stress reduction.

Residual stress in stainless steel is typically confined to a depth of less than 10 μm , and SECM does not introduce additional residual stresses. Additionally, the dissolution process of SUS304 strip can be divided into six stages: (a) Initial oxidation of SUS304 strip (stage 1). (b) Early formation of pitting and grooves, along with rupture of the oxide film (stage 2). (c) Formation of the passive film (stage 3). (d) Rapid expansion of pitting and rupture of the passive film (stage 4). (e) Formation and rapid expansion of honeycomb-like micro-pits (stage 5). (f) Formation of a dissolved surface, accompanied by discharge of electrolyte products (stage 6). From stage 4 to stage 5, with the further increase in machining time, SUS304 strip dissolves quickly, and the quantity of corrosion micro-pits grows. This causes the corrosion regions to expand and gradually merge. Ultimately, honeycomb-like micro-pits at the micrometer level take over the whole machined surface, and the surface layer of cold-rolled SUS304 strip is basically dissolved,

some of the surface stress may be eliminated, leading to a reduction in residual stress on the processed surface when compared to the initial SUS304 surface after rolling. Moreover, in the SECM process using the NaNO_3 solution, the high ionic conductivity of NaNO_3 guarantees an even distribution of current density, resulting in the uniform dissolution of the metal matrix and avoiding local stress concentration. At the same time, the passivation film triggered by NaNO_3 may be able to cover the exposed micro-defects (like micropores and grain boundary gaps) after dissolution, decreasing the stress concentration spots. As a result, surface residual stress is slightly reduced post-electrolysis. The reduction in residual stress also improves the machinability of SUS304 stainless steel, facilitating subsequent processing steps.

3.6.4. Influence of SECM on frictional wear

In the study of the mechanical properties of SUS304 strips, frictional wear not only affects their lifespan and performance but also plays a crucial role in engineering applications [33]. Therefore, the effect of SECM on the frictional wear of SUS304 strips was investigated by examining changes in friction and wear before and after electrochemical processing using a 10 wt% NaNO_3 solution. Figure 10(c) shows the relationship between the friction coefficient and friction time for two sets of samples.

From Figure 10(c), it is evident that the friction coefficient curves for both sets exhibit similar characteristics and can be divided into two distinct stages. In the initial stage, the friction coefficient rises sharply due to the small contact area and high contact stress at the beginning, leading to a rapid increase in friction. In the second stage, the friction coefficient stabilizes due to significant plastic deformation and cold work hardening. As the contact area remains relatively unchanged, the coefficient enters a steady state. By calculating the average friction coefficient during the stable stage for each sample set, the friction coefficient before electrochemical treatment was found to be 0.585, and after treatment, it decreased to 0.533. This indicates that ECM slightly reduces the friction coefficient. The reduction may be attributed to the dual effects of the NaNO_3 solution. One effect is that

the uniform dissolution facilitated by NaNO_3 during the SECM process decreases surface roughness from $\text{Sa } 1.437 \mu\text{m}$ to $\text{Sa } 0.208 \mu\text{m}$, thereby minimizing direct contact between micro-protrusions and the friction pair during the friction process. Additionally, Cr_2O_3 in the passivation film exhibits low-friction properties and may create a "lubricating layer" on the surface of SUS304 strips. This reduces adhesion resistance during wear, markedly improving the friction and wear performance of the machined SUS304 strip.

4. Conclusions

This study explores the electrochemical dissolution behavior of SUS304 stainless steel. A series of quantitative electrochemical tests, such as open circuit potential measurements and polarization curve analysis, was conducted to investigate the anodic dissolution process. Additionally, SECM was applied to machine SUS304 strips. The SECM-machined strips were compared to cold-rolled strips across four aspects: surface roughness, surface hardness, residual stress, and frictional wear. The main findings are summarized as follows:

In ECM tests, the open circuit potential and polarization curves revealed that SUS304 stainless steel exhibits active-passive-transpassive behavior. XPS analysis of the passive film showed it is mainly composed of Fe_2O_3 , FeO , Fe , NbO , Cr_2O_3 , CrO_3 , and Cr . The high content of chromium oxides in the passive layer accounts for its excellent corrosion resistance.

During ECM experiments, the machined surface of SUS304 showed many pits at lower current densities. As the current density increased, the number of pits decreased, resulting in a smoother surface.

Using SECM, the SUS304 strip was machined, and the results showed a significant reduction in surface roughness. Compared with the original surface, the Sa and Sz values decreased by 85.5% and 79.2%, respectively.

The surface hardness values before and after machining were approximately 309 and 313 HV, respectively. The residual stress values were about -191.56 MPa before and -153.08 MPa after machining, while the average friction coefficients were 0.585 and 0.533, respectively. These results indicate that surface hardness, residual stress, and frictional wear characteristics of the SECM-machined strip are largely consistent with those of the cold-rolled strip. This validates SECM as an effective technique for reducing the surface roughness of SUS304 strips without compromising other surface properties. This research is also applicable to SUS304 stainless steel strips with a wide width, characterized by green, cost-effective, and high-quality processing. In the future, to further improve processing efficiency and quality, multi-cathode processing and constant gap machining should be explored.

CRedit authorship contribution statement

Jing Wang: Conceptualization, Formal analysis, Funding acquisition, Writing – original draft. **Wenyun Li:** Resources, Investigation, Data curation. **Xiaokang Yue:** Writing – review & editing. **Zhongkai Ren:** Funding acquisition, Writing – review & editing.

Declaration of competing interest

The authors declare that they have no known competing financial interests or personal relationships that could have appeared to influence the work reported in this paper.

Data availability

Data will be made available on request.

Declaration of generative AI and AI-assisted technologies in the writing process

The authors confirm that there was no use of artificial intelligence (AI)-assisted technology for assisting in the writing or editing of the manuscript and no images were manipulated using AI.

Acknowledgment

This research was sponsored by the National Science Foundation of Shanxi Province of China (No.: 202303021212075), the Special Fund for Science and Technology Innovation Teams of Shanxi Province (No.: 202304051001025), the Xinjiang Institute of Intelligent Equipment (No.: XJYJY2025007), the Open Project of Research Institute of Hai'an-Taiyuan University of Technology (No.: 2024HA-TYUTKFYF010).

References

- Fan, W., Wang, T., Hou, J., Ren, Z., Huang, Q., Wu, G., 2024. Pulsed current-assisted twelve-roll precision rolling deformation of SUS304 ultra-thin strips with exceptional mechanical properties. *International Journal of Extreme Manufacturing*, 6, 045101. <https://doi.org/10.1088/2631-7990/ad4073>
- Wang, T., Wei, X., Zhang, H., Ren, Z., Gao, B., Han, J., Bian, L., 2022. Plastic deformation mechanism transition with solute segregation and precipitation of 304 stainless steel foil induced by pulse current. *Materials Science and Engineering: A*, 840, 142899. <https://doi.org/10.1016/j.msea.2022.142899>
- Zhang, Z., Zhang, H., Liu, X., Wang, T., Huang, Q., Liao, X., 2023. Effect of roll surface topography on microstructure and mechanical properties of 304 stainless steel ultra-thin strip. *Journal of Manufacturing Processes*, 108, 764-778. <https://doi.org/10.1016/j.jmapro.2023.11.014>
- Wan, N., Zhao, B., Ding, W., He, Q., 2025. Research status and tendency on cold expansion anti-fatigue manufacturing technology for aircraft structural fastening holes. *Journal of Manufacturing Processes*, 141, 319-335. <https://doi.org/10.1016/j.jmapro.2025.02.068>
- Zhang, Z., Liao, X., Ren, Z., Wang, Z., Liu, Y., Wang, T., Huang, Q., 2025. Effect of two-pass rolling of textured roll and polished roll on surface topography and mechanical properties of 316L stainless steel ultra-thin strip. *Journal of Iron and Steel Research International*, 32, 186-197. <https://doi.org/10.1007/s42243-024-01219-0>
- Fan, W., Ren, Z., Wei, S., Liu, Q., Wang, T., Wu, G., 2024. Effect of high energy electric pulse on microstructure and mechanical properties of pre-deformed SUS 304 ultra-thin strip. *Materials Science and Engineering: A*, 893, 145364. <https://doi.org/10.1016/j.msea.2023.145364>
- Wang H.B., Song G.L., Tang G.Y., 2016. Effect of electropulsing on surface mechanical properties and microstructure of AISI 304 stainless steel during ultrasonic surface rolling process. *Materials Science and Engineering: A*, 662, 456-467. <https://doi.org/10.1016/j.msea.2016.03.097>
- Xiao, H., Ren, Z., Liu, X., 2017. New mechanism describing the limiting producible thickness in ultra-thin strip rolling. *International Journal of Mechanical Sciences*, 133, 788-793. <https://doi.org/10.1016/j.ijmecsci.2017.09.046>
- Shu, Y., Ren, J., Zhang, W., Liu, W., 2025. Gradient thickness-dependent distribution of residual stress and springback of thin-walled TC4 titanium alloy sheet with variable thickness in collaborative manufacturing process of pre-plastic forming and milling. *The International Journal of Advanced Manufacturing Technology*, 137, 4853-4879. <https://doi.org/10.1007/s00170-025-15429-7>
- Lautre, N.K., Dharmik, B.Y., 2022. Surface integrity and core loss in lamination coated thin sheets of M-43 grade cold rolled non-grain-oriented electrical steel. *Journal of Materials Engineering and Performance*, 31, 9001-9018. <https://doi.org/10.1007/s11665-022-06968-1>
- Zhou, Z., Wang, Y., Liu, Y., Yang, Y., Bao, L., Li, Y., Liu, Y., Yao, J., Zhang, W., 2024. Fiber laser irradiation in chemical solution for micro fabrication: Mechanisms and applications. *Journal of Manufacturing Processes*, 125, 523-537. <https://doi.org/10.1016/j.jmapro.2024.07.115>
- Teng, H., Chen, S., Kurniawan, R., Li, S., Li, C., Xu, M., Chen, J., Ko, T.J., 2025. Brittle-ductile transition model for ultrasonic vibration-assisted blade dicing. *International Journal of Mechanical Sciences*, 293, 110196. <https://doi.org/10.1016/j.ijmecsci.2025.110196>
- Tarafder, P., Xu, J., Wiberg, A., Moverare, J., 2025. Assessing the effect of scan strategies on the structure-property relationship in electron beam powder bed fusion processed 316L stainless steel. *Materials & Design*, 253, 113837. <https://doi.org/10.1016/j.matdes.2025.113837>
- Schuster, R., Kirchner, V., Allongue, P., Ertl, G., 2000. Electrochemical micromachining. *Science (New York, N.Y.)*, 289, 98-101. <https://doi.org/10.1126/science.289.5476.98>
- Rajurkar, K.P., Zhu, D., McGeough, J.A., Kozak, J., De Silva, A., 1999. New developments in electro-chemical machining. *CIRP Annals*, 48, 567-579. [https://doi.org/10.1016/S0007-8506\(07\)63235-1](https://doi.org/10.1016/S0007-8506(07)63235-1)
- Schubert, N., Schneider, M., Michealis, A., 2013. The mechanism of anodic dissolution of cobalt in neutral and alkaline electrolyte at high current density. *Electrochimica Acta*, 113, 748-754. <https://doi.org/10.1016/j.electacta.2013.06.093>
- An, L., Wang, D., Zhu, D., 2022. Combined electrochemical and mechanical polishing of interior channels in parts made by additive manufacturing. *Additive Manufacturing*, 51, 102638. <https://doi.org/10.1016/j.addma.2022.102638>
- Wang, J., Xu, Z., Wang, J., Xu, Z., Zhu, D., 2021. Electrochemical machining of blind channels with rotations of the cathode and the workpiece. *International Journal of Mechanical Sciences*, 208, 106655. <https://doi.org/10.1016/j.ijmecsci.2021.106655>
- Wang, M., Qu, N., 2020. Electrochemical dissolution behavior of S-04 high-strength stainless steel in NaNO_3 aqueous solution. *Journal of Applied Electrochemistry*, 50, 1149-1163. <https://doi.org/10.1007/s10800-020-01469-2>
- Wang, D., Zhu, Z., Wang, N., Zhu, D., Wang, H., 2015. Investigation of the electrochemical dissolution behavior of Inconel 718 and 304 stainless steel at low

- current density in NaNO_3 solution. *Electrochimica Acta*, **156**, 301-307. <https://doi.org/10.1016/j.electacta.2014.12.155>
21. Dong, B., Du, J., Liu, W., Zhao, Y., 2024. Stray current affected zone in electrochemical jet machining. *Surface and Coatings Technology*, **494**, 131413. <https://doi.org/10.1016/j.surfcoat.2024.131413>
 22. Wang, J., Ren, Z., Wang, T., Wang, J., 2025. Scanning electrochemical thinning of strip with smallest rolling thickness. *Materials and Manufacturing Processes*, **40**, 1197-1213. <https://doi.org/10.1080/10426914.2025.2491417>
 23. Zhang, J., Wang, D., Le, H., Fu, T., Zhu, D., 2023. Effect of carbides on the electrochemical dissolution behavior of solid-solution strengthened cobalt-based superalloy Haynes 188 in NaNO_3 solution. *Corrosion Science*, **220**, 111270. <https://doi.org/10.1016/j.corsci.2023.111270>
 24. Chiba, A., Muto, I., Sugawara, Y., Hara, N., 2016. Effect of atmospheric aging on dissolution of MnS inclusions and pitting initiation process in type 304 stainless steel. *Corrosion Science*, **106**, 25-34. <https://doi.org/10.1016/j.corsci.2016.01.022>
 25. Lohrengel, M.M., Rosenkranz, C., 2005. Microelectrochemical surface and product investigations during electrochemical machining (ECM) in NaNO_3 . *Corrosion Science*, **47**, 785-794. <https://doi.org/10.1016/j.corsci.2004.07.023>
 26. Olsson, C.-O.A., Landolt, D., 2003. Passive films on stainless steels—chemistry, structure and growth. *Electrochimica Acta*, **48**, 1093-1104. [https://doi.org/10.1016/s0013-4686\(02\)00841-1](https://doi.org/10.1016/s0013-4686(02)00841-1)
 27. Osório, W.R., Freire, C.M., Garcia, A., 2005. The role of macrostructural morphology and grain size on the corrosion resistance of Zn and Al castings. *Materials Science and Engineering: A*, **402**, 22-32. <https://doi.org/10.1016/j.msea.2005.02.094>
 28. Jiao, E., Zhu, D., Wang, R., Wang, Y., Zhou, X., 2025. Design of insulation sleeve with tensile stress in electrochemical trepanning. *International Journal of Mechanical Sciences*, **299**, 110333. <https://doi.org/10.1016/j.ijmecsci.2025.110333>
 29. Klocke, F., Settineri, L., Lung, D., Claudio Priarone, P., Arft, M., 2013. High performance cutting of gamma titanium aluminides: Influence of lubricoolant strategy on tool wear and surface integrity. *Wear*, **302**, 1136-1144. <https://doi.org/10.1016/j.wear.2012.12.035>
 30. Wang, K., Liu, H., Liu, N., Chen, X., Chen, J., 2024. Effect of oxidant concentration on the oxide layer thickness of 304 stainless steel. *Materials (Basel, Switzerland)*, **17**, 2816. <https://doi.org/10.3390/ma17122816>
 31. Lian, J., Zhao, W., Ma, L., Liao, X., Jiang, Z., Zhao, J., 2025. Effects of combined rolling process on microstructure and wear resistance of 301 stainless steel strips. *Tribology International*, **210**, 110800. <https://doi.org/10.1016/j.triboint.2025.110800>
 32. Cui, C.-H., Zhu, Z.-Q., Chen, Z.-T., Li, Y.-M., 2024. Surface integrity and fatigue life of GH4169 by combined process of milling, grinding, and polishing. *Proceedings of the Institution of Mechanical Engineers Part B Journal of Engineering Manufacture*, **238**, 1914-1923. <https://doi.org/10.1177/09544054231219042>
 33. Lv, B., Chen, Q., Li, Y., Wang, F., Zhang, Y., Han, J., Jiang, Z., Xia, W., 2025. Anisotropy dependence of chip formation and plastic deformation in Fe-25Cr-20Ni austenitic stainless steel during micro-scratching. *Tribology International*, **210**, 110799. <https://doi.org/10.1016/j.triboint.2025.110799>